Published in final edited form as:

Appl Opt. 2016 May 10; 55(14): 3724–3729.

Enabling high-speed wide-field dynamic imaging in multi-focal photoacoustic computed microscopy: a simulation study

Hongying Wan[1], **Yihang Zhou**[1], **Leslie Ying**[1], **Jing Meng**[2], **Liang Song**[3], and **Jun Xia**[1,*]

[1]Department of Biomedical Engineering, University at Buffalo, the State University of New York, Buffalo, NY, 14260, USA

[2]College of Information Science and Engineering, Qufu Normal University, 80 Yantai Road North, Rizhao, Shandong 276826, China

[3]Institute of Biomedical and Health Engineering, Shenzhen Institutes of Advanced Technology, Chinese Academy of Sciences, 1068 Xueyuan Boulevard, Shenzhen 518055, China

Abstract

Photoacoustic-computed microscopy (PACM) is an emerging technology that employs thousands of optical foci to provide wide-field high-resolution images of tissue optical absorption. A major limitation of PACM is the slow imaging speed, limiting its usage in dynamic imaging. In this study, we improved the speed through a two-step approach. First, we employed compressed sensing with partially known support to reduce the transducer element number, which subsequently improved the imaging speed at each optical scanning step. Second, we use the high speed low resolution image acquired without microlens array to inform dynamic changes in the high resolution PACM image. Combining both approaches, we achieved high-resolution dynamic imaging over a wide field.

1. INTRODUCTION

Optical microscopic imaging plays a critical role in biomedical research as it allows for visualization of the biological process with great detail. Among various microscopic modalities, photoacoustic microcopy (PAM) has an unique capability of sensing purely optical absorption [1]. Conventional PAM systems are based on a co-axial design of a single-element acoustic transducer and a single optical focus, and the two raster scan simultaneously within the field of view. The imaging speed of these systems are fundamentally limited by the laser's pulse repetition rate[2–4]. To address this limitation, multi-focal (MF) PAM was proposed[5–7]. The first generation MF-PAM system employed twenty optical foci, while the most recent MF-PAM system, MF-photoacoustic computed microscopy (PACM), combined computed tomography (CT) techniques to allow for simultaneous excitation with thousands of optical foci [6]. However, the inclusion of CT techniques poses additional challenges in imaging speed. For instance, the MF-PACM system contained hundreds of transducer elements, whose data cannot be captured within one laser shot. In addition, the large number of optical foci requires a higher power laser,

*Corresponding author: ; Email: junxia@buffalo.edu

which has limited pulse repetition rate. Because of these, the PACM system in ref. [6] is even slower than conventional PAM systems.

The goal of this study is to improve the imaging speed of MF-PACM based on its unique scanning geometry and image processing procedure. First, we reduce the time required to capture one high resolution image. Because MF-PACM relies on CT-based image reconstruction, we will use compressed sensing (CS) to reduce the transducer element number, which subsequently improves the scanning speed. CS is based on the principle that when an object is sparse in a certain domain, the imaging system will be able to reasonably recover the object in an under-sampled fashion [8–10]. Because of the sparsely distributed optical foci, MF-PACM naturally meets the sparsity requirement. In addition, the known optical foci arrangement can be used as partially known support (PKS) to further improve the image quality. By using PKS, we can enforce the CS minimization to be conducted only outside the optical foci, thus the signals inside optical foci are preserved. After acquiring a high resolution image, we will use a fundamentally new approach to improve the dynamic imaging speed. Because the MF-PACM system can be converted into a photoacoustic computed tomography (PACT) system by simply removing the microlens array, we will use the high-speed PACT system, which can acquire one image after each laser pulse, to capture the dynamic changes, and then map these changes to the high resolution reference image. This approach is applicable to most dynamic PAM studies where the main structure (blood vasculature) remains stationary and only the pixel intensity changes (due to, for instance, functional changes in oxygen saturation [11] or perfusion of a contrast agent). Combining these approaches, we will enable real-time dynamic imaging in MF-PACM.

2. BACKGROUNDS AND METHODS

A. Backward and forward models for PA imaging

Photoacoustic imaging is based on the photoacoustic effect, where optical absorption is converted into acoustic energy through thermal elastic expansion. Because optical scattering does not induce any acoustic signal, photoacoustic imaging is only sensitive to optical absorption. Common endogenous tissue absorbers are hemoglobin, lipid and water.

Once an object absorbs optical energy, it induces an initial pressure rise $p_0(\vec{r'})$, which then propagates through tissue and can be detected by ultrasound transducers placed around the object. The received signal at detector location $\vec{r}$ is determined by the following forward model [12]

$$p(\vec{r},t)=\frac{\partial}{\partial t}\left[\frac{1}{4\pi c^3 t}\int d\vec{r}' p_0(\vec{r}')\delta\left(t-\frac{|\vec{r}-\vec{r}'|}{c}\right)\right], \quad (1)$$

where c is the speed of sound, t is the signal propagation time, and $\vec{r'}$ is the location of initial pressure. Reversing the process (backward model) allows for recovering the initial pressure based on the detected signal. For three canonical detection geometries, i.e., planar, cylindrical and spherical, the universal back-projection (BP) algorithm provides an exact analytical solution to the reverse problem [12]:

$$p_0(\vec{r}) = \int_{S_0} [2p(\vec{r}_0, \bar{t}) - 2\bar{t}\partial p(\vec{r}_0, \bar{t})/\partial t]|_{\bar{t}=|r-r_0|} d\Omega_0/\Omega_0. \quad (2)$$

Here S_0 is the receiving aperture, $\bar{t} = ct$, $d\Omega_0/\Omega_0$ is the solid angle weighting factor, and $-2\bar{t}\partial p(\vec{r_0}, \bar{t})/\partial t$ denotes the filter that suppress low frequency components [12].

To better mimic the experimental condition, we convolved the simulated signals with a temporal impulse response of a real transducer (by illuminating the transducer surface with a 10 ns pulsed laser). The impulse function works as a filter to suppress the signal at very low and high frequency ends. Thus the second component of Eq. (2) can be removed. It should be noted that, strictly speaking, the universal back projection algorithm cannot be used in the circular detection geometry in MF-PACM. However, because the array is cylindrically focused to receive only in-plane signals, we can still use Eq. (2) as an approximation.

B. CS-PKS-based image reconstruction

1. CS image reconstruction for data acquired at each scanning step—Reducing transducer elements may eliminate the need of multiplexing in data acquisition, which subsequently improves the imaging speed. However, the under sampled data may also cause severe streaking artifacts. CS can be used to address this issue. To use CS, we need to meet two basic CS requirements: (1) the image needs to be sparse or sparse in a transformed domain, and (2) the measurement matrix need to be incoherent with the sparse basis of the image [8]. MF-PACM meets both requirements because (1) the microlens array naturally forms a sparse image due to the sparsely distributed optical foci, and (2) the measurement is a linear combination of the sparse image obtained from a ring transducer array with elements uniformly distributed over 360°.

The basic concept of CS can be described as:

$$\min_x \|\Psi x\|_1 \text{s.t.} \|\Phi x - y\|_2 < \varepsilon. \quad (3)$$

Here Ψ is the sparsity transforming matrix (in our case is the identity matrix), x is the reconstructed image of the object, Φ is the forward model, y indicates the detected raw data, and ε is the estimated noise level. $\Phi x - y$ denotes the error between the real raw channel data and the calculated raw data obtained from the forward model. $\|x\|_1$ and $\|x\|_2$ are ℓ_2 norm (defined as $\|x\|_1 = \sum |x_i|$) and ℓ_2 norm (defined as $\|x\|_2 = \sqrt{\sum |x_i|^2}$), respectively [9]. For computer implementation, Eq. (3) can be further written as:

$$\min_x \|\Phi x - y\|_2^2 + \lambda \|x\|_1. \quad (4)$$

The first part of this equation denotes the data consistency and the second part denotes the sparse representation of the object. Here, λ is a parameter determining the trade-off between sparsity and data consistency. Thus the goal of CS is to enforce sparsity while maintaining data consistency. Eq. (4) is typically solved using a iteratively reweighed conjugate gradient descent (IR-CGD) algorithm [13, 14].

2. CS-PKS image reconstruction for data acquired at each scanning step—CS with partially known support (PKS) takes into account of prior information about the locations of nonzero signals, which needs to be excluded from the minimization procedure. PKS can be introduced into CS by modifying Eq. (4) into:

$$\min_x \|\Phi x - y\|_2^2 + \lambda \|x_\Delta\|_1. \quad (5)$$

where x_Δ denotes signals located outside the known (nonzero) region (T_0).

For MF-PACM, because photoacoustic signals can only be generated within the optical foci, locations of the optical foci can be used as the known support P_0. Additional support at the i^{th} iteration can be determined through thresholding [14, 15]:

$$T_0^{(i)} = \left\{ z : x_z^{(i)} > \tau^{(i)} \right\}. \quad (6)$$

Here $x_z^{(i)}$ is the z^{th} pixel intensity (positive) of reconstructed image in the i^{th} iteration. Threshold $\tau^{(i)}$ is set by $\tau^{(i)} = \|x^{(i)}\|_\infty / \delta$, where δ is a parameter (set to 3 in our simulation) that can be adjusted and $\|x^{(i)}\|_\infty$ indicates the maximum value of $x^{(i)}$. Combining with optical foci location, the known support at each iteration is given by:

$$T_0^{(i)} = \left\{ z : x_z^{(i)} > \tau^{(i)} \cap z \in P_0 \right\}. \quad (7)$$

Based on Eq. (7), we can create a 2D matrix M with the same size of image x. In M, pixels inside the known region are set to 0 whereas others are set to 1. Eq. (5) can then be further written as

$$\min_x \|\Phi x - y\|_2^2 + \lambda \|M^{(i)} x\|_1. \quad (8)$$

For images presented in the Results and Discussion sections, parameters λ in Eqs. 4 and 8 have been adjusted based on visual assessment between reconstructed image and the gold standard to render the best result.

C. Combining raster-scan images to form a high resolution image in MF-PACM

In PACM, a high resolution image is formed by combining low resolution images acquired at each scanning step. However, simply adding up all low resolution images will not improve the spatial resolution. We need to first filter each image into a higher resolution [6]. The filtering process works in a similar way as the PKS. Based on the microlens array position at each scanning step j, we create a matrix $F^{(j)}$ with pixel size equaling the optical focus diameter. In F, pixels inside optical foci have a value of 1 whereas others equal 0. We then interpolate the low resolution image to the same pixel size of the matrix F and multiple the two. This operation acts as a high pass filter, which subsequently improves the image resolution at each scanning step up to the optical focal diameter. Combining filtered images of all scanning steps then yields a high resolution image H_0. This process can be expressed in Eq. (9).

$$H_0=\sum_{j=1}^{J} I^{(j)}F^{(j)} \quad (9)$$

Here J is the total number of scanning steps, and $I^{(j)}$ refers to the interpolated low resolution image of the j^{th} scanning step.

D. Reconstruction of high-resolution dynamic images

For dynamic imaging, we remove the microlens array and convert the microscopic system into a conventional circular-view PACT system [16]. This modification allows us to acquire one low resolution image after each laser shot. Dynamic changes will be derived from these low resolution images and mapped to the high resolution image.

1. Reconstruction of low resolution dynamic images—To obtain high quality low resolution images, we employ the low-rank matrix estimation-based spatiotemporal image reconstruction (LRME-STIR) algorithm [17]. Unlike conventional frame-by-frame image reconstruction (FBFIR), in which each frame is computed individually, LRME-STIR takes into account correlations among data frames. This is done through the singular value decomposition (SVD) of data matrix G. For a low rank data matrix G, the main statistical features are kept only on the first few singular components. Reconstructing these large components allows for a more efficient and accurate recovery of dynamic features. Detailed derivation of LRME-STIR can be find in ref. [17].

2. Mapping low resolution dynamic changes into high resolution image—For most photoacoustic dynamic imaging applications, such as monitoring the perfusion of a contrast agent [18] or functional changes in oxygenation saturation [19], the object is stationary and only the pixel intensity changes. In this case, we can extract dynamic changes from the low-resolution PACT system and map them into a high resolution PAM image. The hybrid nature of PACM readily allows this implementation. To extract dynamic changes, we will divide each frame of low resolution image by a static low resolution image. This operation provides rational dynamic changes at each frame:

$$\{D\}_{n=1}^{N}=\frac{\{L\}_{n=1}^{N}}{L_1}, 1<\{D\}_{n=1}^{N}<\tau_m \quad (10)$$

Here $\{L\}_{n=1}^{N}$ are the N frames of low resolution dynamic images reconstructed by LRME-STIR, and L_1 is the static low resolution image, which contains only structural information. Thus $\{D\}_{n=1}^{N}$ denotes dynamic changes in ratio. To avoid extremely large ratios generated by a small denominator, such as noise, we set an upper limit τ_m. Also, in the simulation, we defined the rational changes to be larger than 1, so we also set a lower limit of 1.

Multiplying the rational changes with a high resolution static image (obtained before removing the microlens array) gives dynamic changes at high resolution. This procedure can be described by Eq. (11).

$$\{\mathrm{H}\}_{n=1}^{N}=\{\mathrm{D}\}_{n=1}^{N}\cdot \mathrm{H}_0. \quad (11)$$

Here H_0 is the high resolution static image acquired with microlens array.

3. RESULTS AND DISCUSSION

Simulations are conducted to verify the aforementioned methods. All methods are implemented in Matlab (MathWorks, Natick, MA).

The simulated MF-PACM system is based on Ref. [6]. Fig. 1(a) shows a schematic drawing of the system in top view. In this MF-PACM system, the optical and acoustic axes are orthogonal to each other, which allows for the accommodation of thousands of optical foci. The ring-shaped transducer array used in Ref. [6] contained 512 elements. Because a 512-channel DAQ was not commercially available, 8:1 multiplexed data acquisition was needed, which degraded the imaging speed. In this study, we aim to decrease the transducer element number to 128 (128-channel DAQs are commercially available from several vendors, such as Ultrasonix and Verasonics) and use CS-PKS to improve the reconstruction quality. This will improve the imaging speed of the original MF-PACM system by four times (when both systems use a 128-channel DAQ). To ensure compliance with the basic CS requirement, the 128 elements will be uniformly distributed around the ring array [Fig. 1(b)]. The simulated microlens array has 40×40 optical foci over a 10×10 mm^2 region. Raster scanning 100 steps yields 100 frames of partial optical resolution images. A high resolution image can be produced by combining these 100 frames (Method section C).

Object used in our simulation is a leaf skeleton image (10×10 mm^2) [Fig. 2(a)]. In this image, blue corresponds to zero optical absorption, while yellow represents high optical absorption. The effect of microlens array is simulated using a 10×10 mm^2 mask with pixel size equaling the optical focus diameter (25 μm)[Fig. 2 (b)]. In this mask, pixels inside the optical foci are set to one and pixels outside the optical foci are set to zero. Multiplying this mask with the original object mimics MF-PACM signal generation: only objects within optical foci generate an initial pressure rise $p_0(\vec{r'})$ [Eq. (1)]. Raster scanning of microlens array is simulated by shifting the mask position according to the scanning direction and step size (25 μm). A 10 by 10 raster scan generates 100 raw datasets.

We first compare images acquired at one scanning step using different reconstruction methods [Fig. 3]. Fig. 3(a) is captured with 512 elements and reconstructed using the back-projection method. Figs. 3(b)–(d) are images captured with 128 elements and reconstructed using back-projection, basic CS [Eq. (4)], and CS-PKS [Eq. (8)] methods, respectively. Due to the reduction in transducer elements, Fig. 3(b) shows strong streaking artifacts. The artifacts are slightly suppressed in the conventional CS reconstruction [Fig. 3(c)] and are significantly mitigated in the CS-PKS reconstruction [Fig. 3(d)] due to the utilization of optical foci information.

We then combine images of all scanning steps to form a high resolution image (Method Section C). Results, shown in Figs. 4(a)–(d), are reconstructed using the same methods as Figs. 3(a)–(d), respectively. It can be seen that while Fig. 4(a) recovers all the vascular

structures, the image is contaminated by shadowing artifacts at the vessel boundaries. Fig. 4(b) is severely contaminated by under sampling artifacts, shown as strong negative signals in regions without any vessels. While the basic CS reconstruction [Fig. 4(c)] suppresses some artifacts, the primary signal intensity has also been degraded. For the CS-PKS reconstructed image [Fig. 4(d)], most artifacts disappear and the image represents the gold standard [Fig. 2(a)] very well.

To further quantify the image quality, we calculated the signal to noise ratio (SNR) of each image in Fig. 4. The SNR is determined by $\bar{a}_s/SD_n$, where $\bar{a}_s$ is the mean density of the region containing signal (vessel) and SD_n is the standard deviation of the background region. The signal and background regions are differentiated by a threshold of 20%, i.e., pixels with amplitude above 20% of the maximum are treated as signal while the others are treated as noise. Besides image quality, we also calculated the structural similarity (SSIM) [20] index between the reconstructed image and the gold standard (original leaf skeleton). The SNR and SSIM results are shown in Table 1. It can be seen that the SNR and SSIM of CS-PKS are constantly ranked in the first. This table further demonstrates that the proposed CS-PKS algorithm is efficient in recovering high quality images from under-sampled data.

We then investigate the efficiency of our dynamic imaging method. To generate dynamic images, we multiply the vessel image [Fig. 2(a)] with 30 masks which mimic the perfusion of a dye from the bottom left region to the entire image over 30 frames [Fig. 5]. As mentioned previously, for dynamic imaging, our goal is to extract the dynamic changes from the high-speed low-resolution images and map them into the high-resolution static image reconstructed by CS-PKS. To ensure that the low resolution image contains the key dynamic information, we use the LRME-STIR algorithm (Method Section D). We then extract the dynamic changes in ratio and map them to the high resolution static image [Eqs. (10)–(11)]. The mapped results are shown in Figs. 6(a)–(d).

For comparison, we also multiple the high resolution image with the true perfusion mask [Fig. 5]. The results are shown in Figs. 6(e)–(h) as gold standards. It can be seen that temporal changes in the top and bottom rows agree very well. This result demonstrates that we can use the high-speed low-resolution image to inform changes at high resolution.

To further qualify the accuracy of dynamic changes, we compare our result with dynamic changes extracted from FBFIR. The two groups of rational changes are multiplied by the high resolution image [Fig. 4(d)], and then we calculate the SSIM index between these two groups of images and the gold standards (high resolution image multiplied by the true perfusion mask). If the reconstructed dynamic images exactly represent the gold standards, the SSIM index should be 1. However, because of noise introduced through the impulse response of a real transducer, it is hard to achieve those ideal values. Figure 7 shows the results. As expected, LRME-STIR's SSIM indexes are much closer to 1. This means that the LRME-STIR algorithm reconstruct dynamic changes better than the conventional FBFIR algorithm. For both cases, there is a slight drop in SSIM at the middle few frames. This could be caused by the fact that these frames have a static-to-dynamic ratio of close to one. However, the reconstruction algorithm tends to distribute energies more evenly throughout

the reconstructed space, causing discrepancies in SSIM. Nevertheless, the changes are small (<5%) and will not degrade the dynamic imaging quality.

4. CONCLUSION

We successfully used two techniques to improve the speed of MF-PACM. The first technique, CS-PKS, utilizes the sparse optical foci distribution in MF-PACM to reduce the transducer array elements and subsequently improves the imaging speed by four times without compromising the image quality. In fact, the introduction of PKS even reduces the shadowing artifacts in the original 512-element reconstructed image. To further improve the dynamic imaging speed, we took advantage of the hybrid nature of MF-PACM. We first removed the microlens array to capture dynamic changes at high speed with low spatial resolution. Then we reconstructed data using LRME-STIR, which suppressed noise and preserved main dynamic features among frames. Finally, we extracted the dynamic information from these low resolution image frames and mapped them to the high resolution MF-PACM image. Combining both techniques, we achieved high-speed wide-field dynamic imaging in MF-PACM. For future work, we can further improve the imaging speed by reducing raster scanning steps. This can be done through image in painting [21]. For better recovery of dynamic changes in small structures, such as capillaries, we may also implement selective scan of microlens array at certain regions, which has been achieved by digital micro device (DMD) in conventional PAM [22]. Combining all these improvements, MF-PACM can be used to capture fast dynamic changes over a large field, and we expect it to have wide applications in biomedical research.

Acknowledgments

Funding. University at Buffalo startup funding; the SUNY Brain Network of Excellence “Big Idea” Award; National Institutes of Health (R21EY026411); and National Natural Science Foundation of China (NSFC) (61308116)(J. M.).

REFERENCES

1. Yao J, Wang LV. Photoacoustic microscopy. Laser & Photonics Reviews. 2013; 7:758–778.
2. Rao B, Li L, Maslov K, Wang L. Hybrid-scanning optical-resolution photoacoustic microscopy for in vivo vasculature imaging. Optics letters. 2010; 35:1521–1523. [PubMed: 20479795]
3. Wang L, Maslov K, Yao J, Rao B, Wang LV. Fast voice-coil scanning optical-resolution photoacoustic microscopy. Optics letters. 2011; 36:139–141. [PubMed: 21263479]
4. Yao J, Huang C-H, Wang L, Yang J-M, Gao L, Maslov KI, Zou J, Wang LV. Wide-field fast-scanning photoacoustic microscopy based on a water-immersible MEMS scanning mirror. Journal of biomedical optics. 2012; 17:0805051–0805053.
5. Song L, Maslov K, Wang LV. Multifocal optical-resolution photoacoustic microscopy in vivo. Optics letters. 2011; 36:1236–1238. [PubMed: 21479041]
6. Xia J, Li G, Wang L, Nasiriavanaki M, Maslov K, Engelbach JA, Garbow JR, Wang LV. Wide-field two-dimensional multifocal optical-resolution photoacoustic-computed microscopy. Optics letters. 2013; 38:5236–5239. [PubMed: 24322226]
7. Li G, Maslov KI, Wang LV. Reflection-mode multifocal optical-resolution photoacoustic microscopy. J. Biomed. Opt. 2013; 18 030501-030501.
8. Liang D, Zhang HF, Ying L. Compressed-sensing photoacoustic imaging based on random optical illumination. International Journal of Functional Informatics and Personalised Medicine. 2009; 2:394–406.

9. Guo Z, Li C, Song L, Wang LV. Compressed sensing in photoacoustic tomography in vivo. Journal of Biomedical Optics. 2010; 15 021311-021311-021316.

10. Meng J, Wang LV, Liang D, Song L. In vivo optical-resolution photoacoustic computed tomography with compressed sensing. Optics letters. 2012; 37:4573–4575. [PubMed: 23164842]

11. Wang L, Maslov K, Wang LV. Single-cell label-free photoacoustic flowoxigraphy in vivo. Proceedings of the National Academy of Sciences. 2013; 110:5759–5764.

12. Xu, M.; Wang, LV. Biomedical Optics 2005. International Society for Optics and Photonics; 2005. Universal back-projection algorithm for photoacoustic computed tomography; p. 251-254.

13. Figueiredo MA, Nowak RD, Wright SJ. Gradient projection for sparse reconstruction: Application to compressed sensing and other inverse problems. Selected Topics in Signal Processing, IEEE Journal of. 2007; 1:586–597.

14. Meng J, Wang LV, Ying L, Liang D, Song L. Compressed-sensing photoacoustic computed tomography in vivo with partially known support. Optics Express. 2012; 20:16510–16523.

15. Liang D, DiBella EV, Chen RR, Ying L. k-t ISD: Dynamic cardiac MR imaging using compressed sensing with iterative support detection. Magnetic resonance in medicine. 2012; 68:41–53. [PubMed: 22113706]

16. Gamelin J, Maurudis A, Aguirre A, Huang F, Guo P, Wang LV, Zhu Q. A real-time photoacoustic tomography system for small animals. Opt. Express. 2009; 17:10489–10498. [PubMed: 19550444]

17. Wang K, Xia J, Li C, Wang LV, Anastasio MA. Fast spatiotemporal image reconstruction based on low-rank matrix estimation for dynamic photoacoustic computed tomography. Journal of biomedical optics. 2014; 19 056007-056007.

18. Li C, Aguirre A, Gamelin J, Maurudis A, Zhu Q, Wang LV. Real-time photoacoustic tomography of cortical hemodynamics in small animals. J. Biomed. Opt. 2010; 15 010509-010501-010503.

19. Xia J, Danielli A, Liu Y, Wang L, Maslov K, Wang LV. Calibration-free quantification of absolute oxygen saturation based on the dynamics of photoacoustic signals. Opt. Lett. 2013; 38:2800–2803. [PubMed: 23903146]

20. Wang Z, Bovik AC, Sheikh HR, Simoncelli EP. Image quality assessment: from error visibility to structural similarity. Image Processing, IEEE Transactions on. 2004; 13:600–612.

21. Bertalmio, M.; Sapiro, G.; Caselles, V.; Ballester, C. Proceedings of the 27th annual conference on Computer graphics and interactive techniques. Addison-Wesley Publishing Co: ACM Press; 2000. Image in painting; p. 417-424.

22. Liang J, Zhou Y, Winkler AW, Wang L, Maslov KI, Li C, Wang LV. Random-access optical-resolution photoacoustic microscopy using a digital micromirror device. Optics letters. 2013; 38:2683–2686. [PubMed: 23903111]

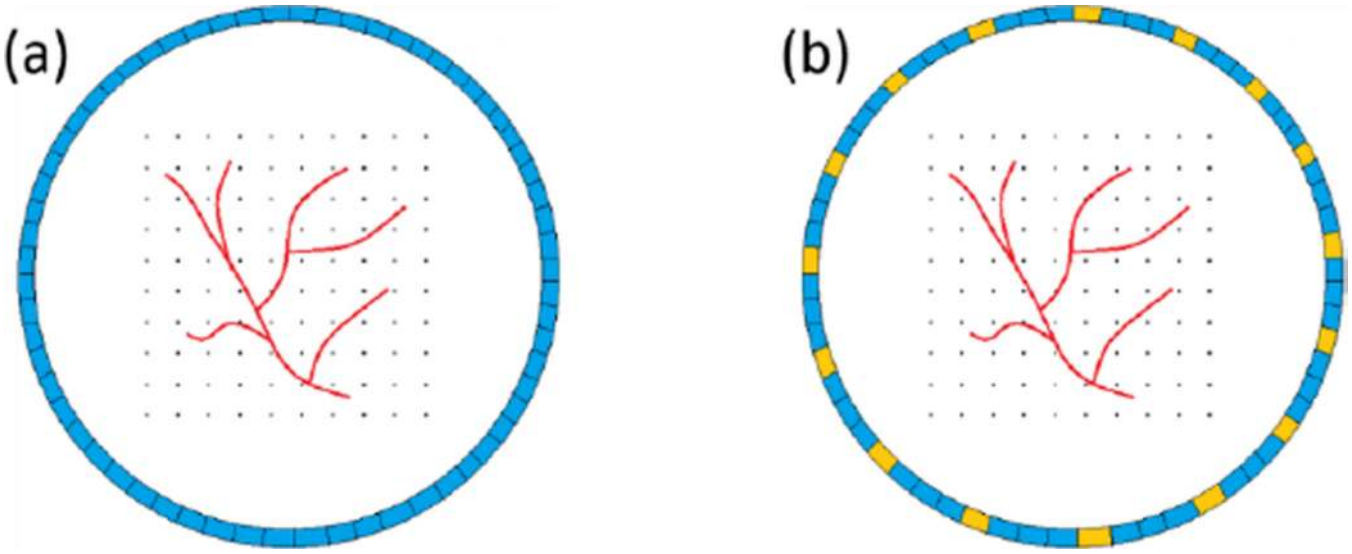

Fig. 1.

Schematic drawing of the MF-PACM system. Black dots indicate optical foci. The blood vasculature is shown in red. (a) MF-PACM system with 512 elements; (b) MF-PACM system with 128 elements (yellow), obtained by selecting one out of every four elements in the 512-element array. For simplicity, not all transducer elements and optical foci are drawn here.

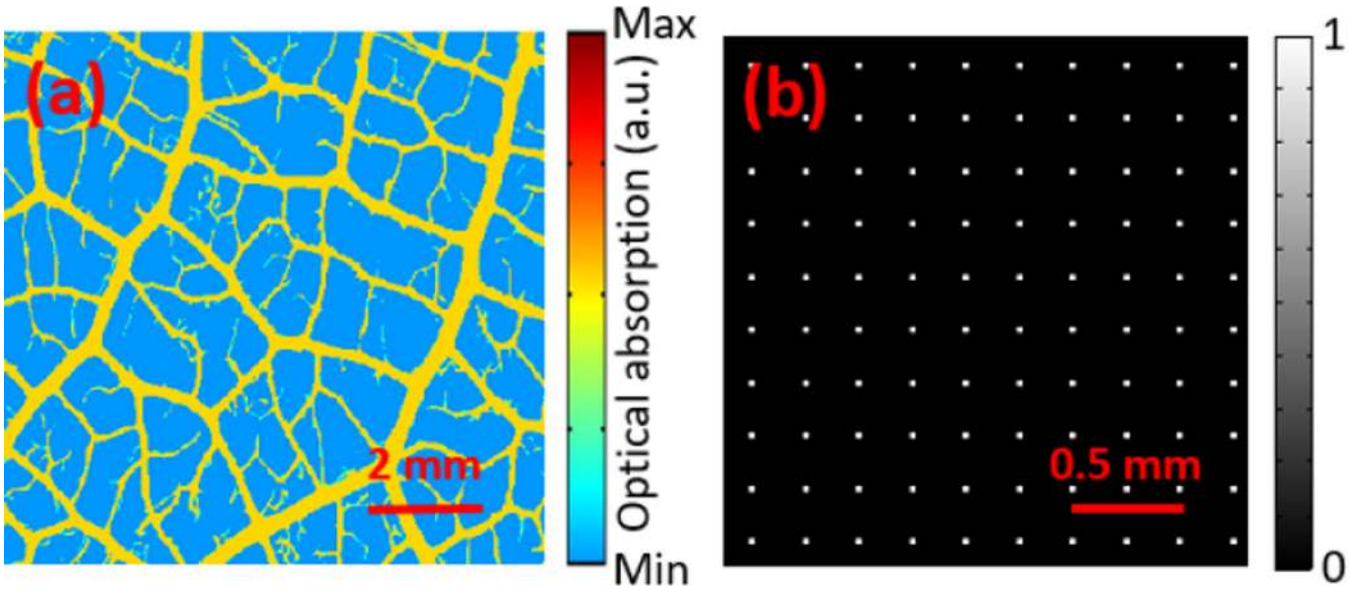

Fig. 2.

(a) Original object, yellow indicates high optical absorption, while blue indicates low optical absorption. (b) Mask for the simulated optical foci. For simplicity, only a small portion of the mask is shown here.

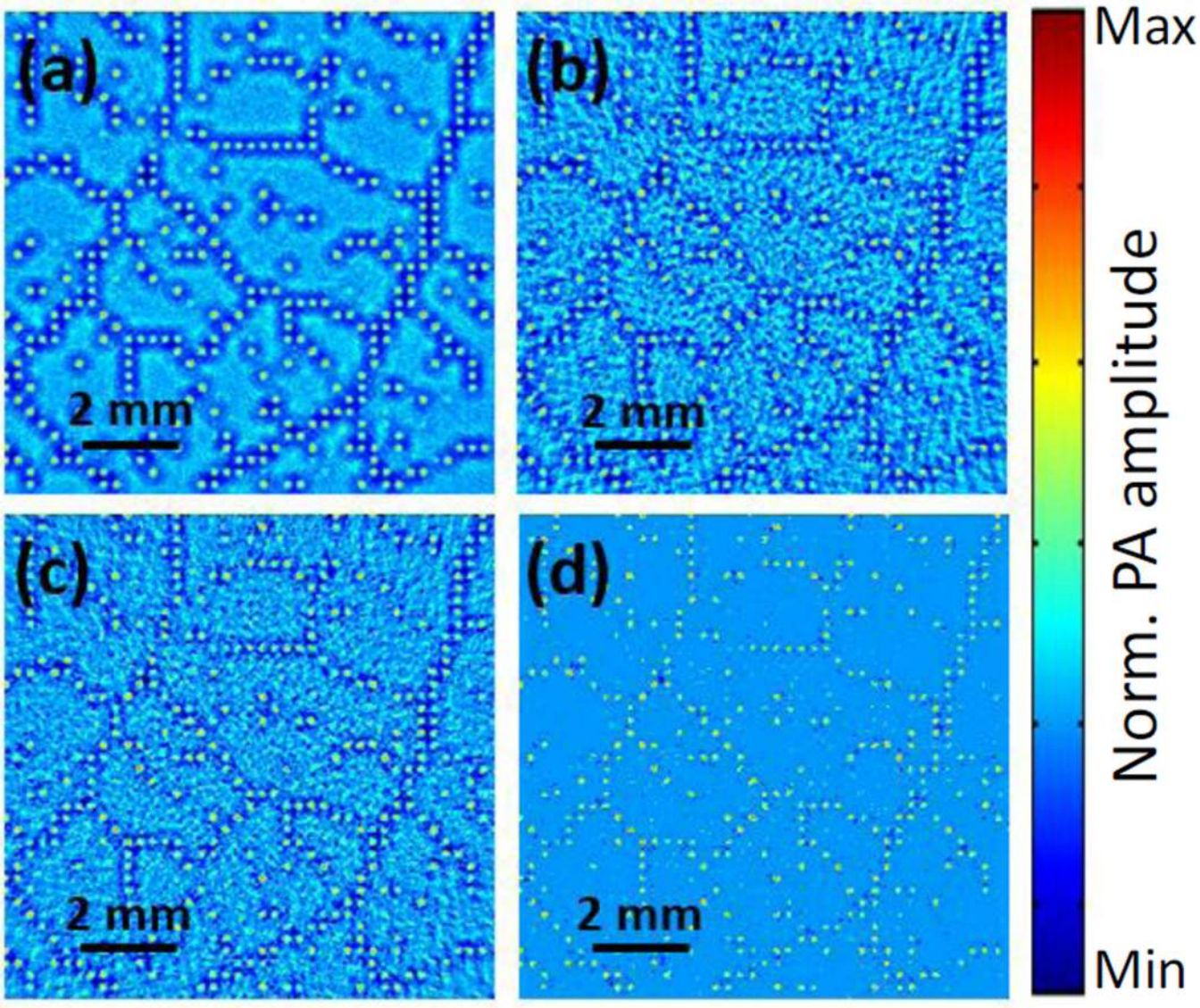

Fig. 3.

Comparison of images acquired at one micro-lens array scanning step. (a) BP-reconstructed image of data acquired from 512 transducer elements. (b) BP-reconstructed image of data acquired from 128 transducer elements. (c) CS-reconstructed image of data acquired from 128 transducer elements. (d) CS-PKS-reconstructed image of data acquired from 128 transducer elements.

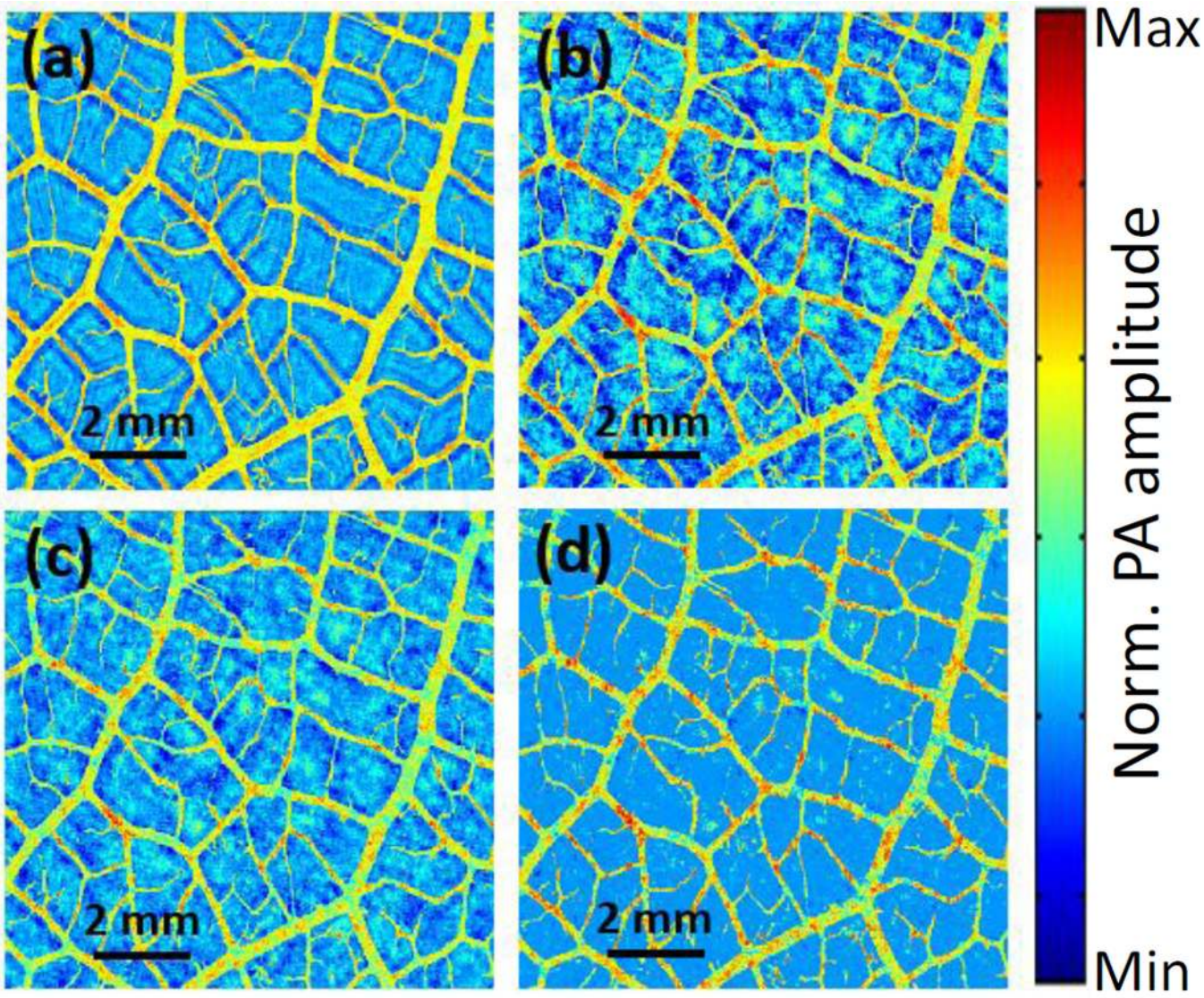

Fig. 4.

Combined high-resolution images for data acquired from (a) 512 elements and reconstructed with the BP algorithm, (b) 128 elements and reconstructed with the BP algorithm, (c) 128 elements and reconstructed with the basic CS algorithm, and (d) 128 elements and reconstructed with the CS-PKS algorithm.

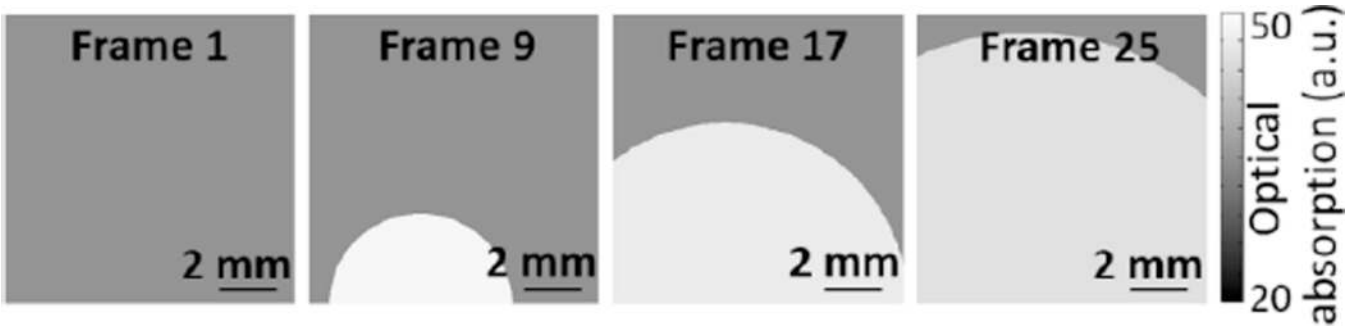

Fig. 5.
Perfusion masks.

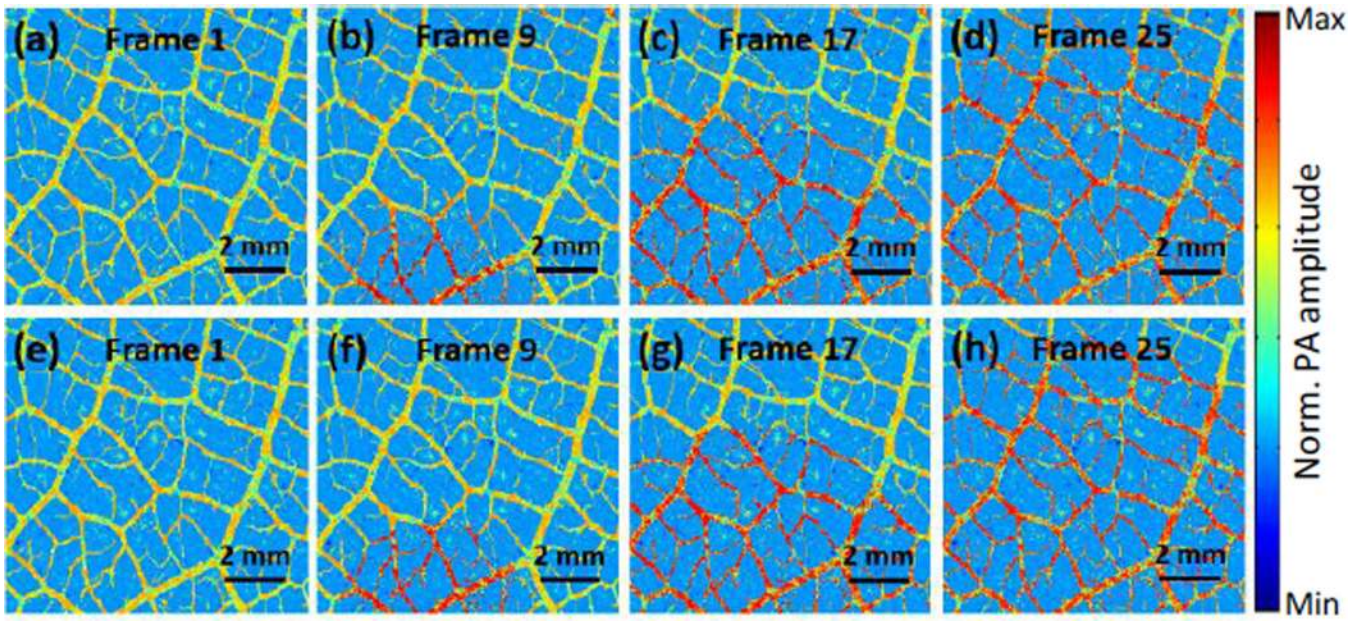

Fig. 6.

(a)–(d) High resolution dynamic images derived based on Eq. 11. (e)–(h) The Gold standard, generated by multiplying the high resolution static image with the true perfusion mask in Fig. 5.

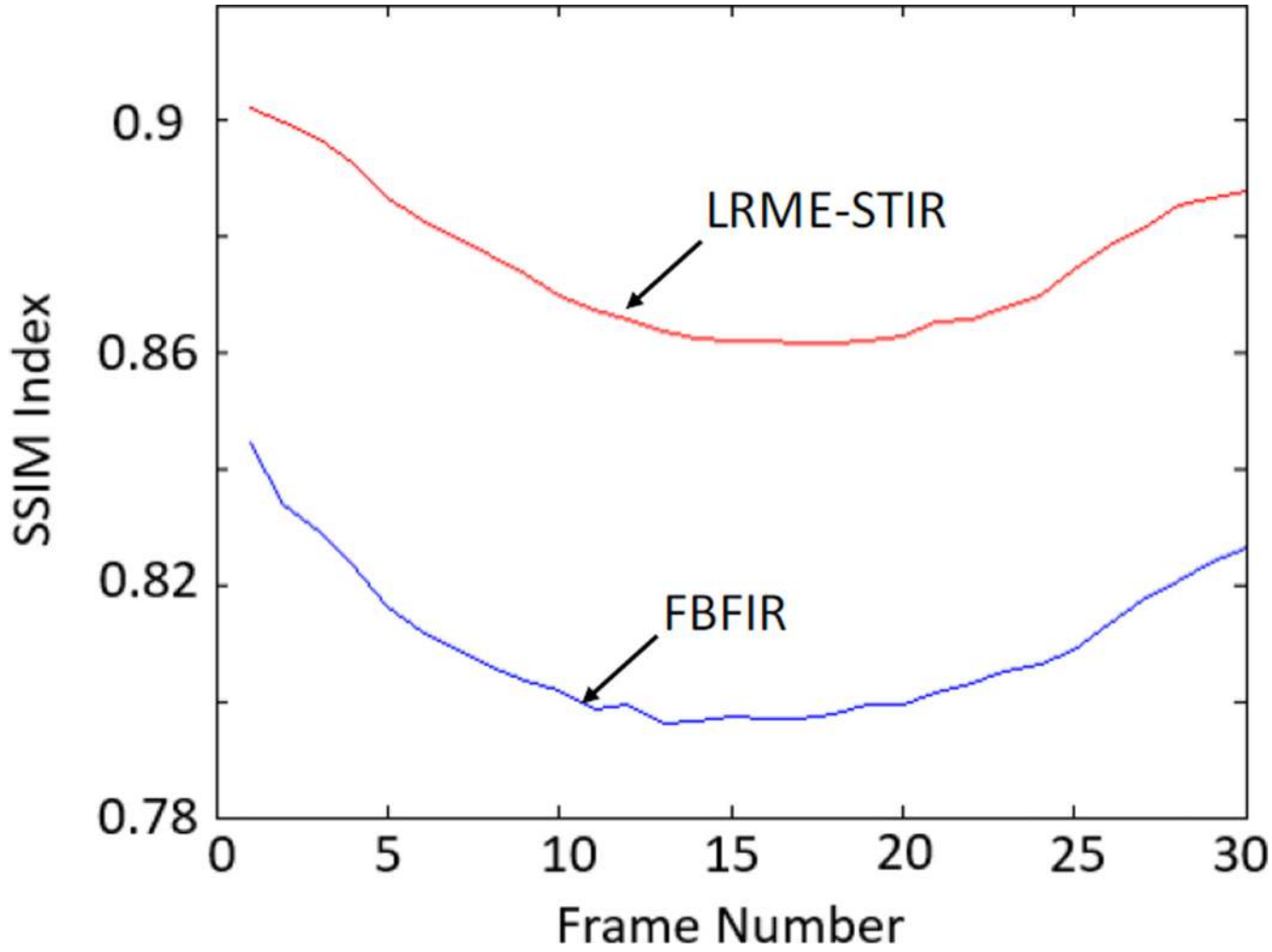

Fig. 7.

Comparison of SSIM index of high resolution dynamic images with dynamic changes extracted from FBFIR and LRME-STIR.

Table 1

SNRs and SSIMs for images reconstructed by different algorithms

	SNR	SSIM
512 BP	8.71	0.28
128 BP	4.33	0.18
128 basic CS	5.29	0.19
128 CS-PKS	15.89	0.60